



**Repositorio Institucional de la Universidad Autónoma de Madrid**

<https://repositorio.uam.es>

Esta es la **versión de autor** del artículo publicado en:

This is an **author produced version** of a paper published in:

ACS Applied Energy Materials 3.2 (2020): 1922-1932

**DOI:** <https://doi.org/10.1021/acsaem.9b02339>

**Copyright:** © 2020 American Chemical Society

El acceso a la versión del editor puede requerir la suscripción del recurso

Access to the published version may require subscription

# Ultrathin transparent B-C-N layers grown on titanium substrates with excellent electro-catalytic activity for the oxygen evolution reaction

*Nuria Jiménez-Arévalo<sup>1,†</sup>, Fabrice Leardini<sup>1,2,\*†</sup>, Isabel Jiménez Ferrer<sup>1,2</sup>, José Ramón Ares<sup>1</sup>, Carlos Sánchez<sup>1,2</sup>, Mahmoud M. Saad Abdelnabi<sup>3</sup>, Maria Grazia Betti<sup>3</sup>, Carlo Mariani<sup>3</sup>*

<sup>1</sup> Departamento de Física de Materiales, Universidad Autónoma de Madrid, Campus de Cantoblanco E-28049, Madrid, Spain

<sup>2</sup> Instituto Nicolas Cabrera, Universidad Autónoma de Madrid, Campus de Cantoblanco E-28049, Madrid, Spain

<sup>3</sup>Dipartimento di Fisica, Università di Roma 'La Sapienza', I-00185 Roma, Italy

**Keywords:** plasma-enhanced chemical vapor deposition, Borocarbonitride, water splitting, electrocatalysis, photocatalysis, x ray photoelectron spectroscopy

## Abstract

Ultrathin B-C-N layers grown on Ti substrates are investigated as efficient anodes for electrochemical water splitting. A fast and direct synthetic route has been used, based on plasma-enhanced chemical vapour deposition with Methylamine Borane as a single-source molecular precursor. The effect of growth time on the morphological and structural properties and on the chemical composition of the layers has been investigated by scanning electron microscopy, Raman spectroscopy, x-ray photoelectron spectroscopy and transmission electron microscopy coupled with electron energy loss spectroscopy. Flat B-C-N layers on top of an amorphous titanium oxide layer present at the Ti surface have been obtained by using short growth times, while longer growth times give rise to core/shell structures formed by vertical wall B-C-N layers and titanium carbonitride phases. The obtained layers present enhanced electrocatalytic activity for the oxygen evolution reaction in alkaline aqueous solutions. Moreover, owing to their ultrathin nature, the B-C-N layers preserve the photocurrents of the underlying titanium oxide layer, acting as transparent electrodes with

high conductivity for the photogenerated charge carriers and improved electrocatalytic activity for the oxidation of water to oxygen gas.

## 1. Introduction

The implementation of renewable energy resources is one of the main issues in the global agenda, due to environmental, economic and geostrategic concerns. The achievement of this goal is closely related to the development of energy storage technologies at large scale, such as power to gas technologies. In this way, electric energy surpluses coming from wind farms or solar-electric generation parks can be stored in the form of a synthetic fuel. The simplest way of doing so is by splitting water molecules by electrolysis to generate hydrogen (the energy carrier) and oxygen. Other approaches are based on the direct use of solar light to dissociate water molecules by photolysis or the synergetic use of electricity and sun light by photo-electrolysis.

The overall water splitting reaction consists in two partial-reactions taking place at the cathode and the anode of the (photo-) electrolytic cell: hydrogen and oxygen evolution reactions (HER and OER, respectively). OER is much more complicated as compared to the HER, since it involves the transfer of four electrons along with the cleavage of O-H bonds and the generation of dioxygen double bonds, and it is usually the rate-determining step of the overall water splitting reaction [1-3]. Actually in many cases sacrificial electron donors (hole scavengers) are added to the electrolytes when investigating the photolytic or photo-electrolytic HER [4], due to the sluggish nature of the OER. However, this approach does not produce the dissociation of water molecules into  $H_2$  and  $O_2$ . Instead of that, it generates  $H_2$  and the oxidation of the sacrificial agent, which is consumed during the reaction and thus can limit the overall reaction due to its depletion. Therefore, in order to achieve the water dissociation reaction, a (photo-) anode material able to sustain the OER is needed.

The development of novel electro- and photo-catalysts based on metal-free, cheap and abundant elements is a big challenge. At recent times, ternary borocarbonitride compounds (BCNs hereafter) have emerged as active electrocatalysts for the HER [5-8], as well as for the oxygen reduction reaction (ORR) [7-9]. Moreover, BCNs have shown interesting photocatalytic properties for hydrogen generation [10,11]. However, there are few works focusing on the OER properties of BCNs. As far as we know, there is only one previous

paper dealing with the synergetic use of  $\text{Co}_3\text{O}_4$ -BCN hybrid catalysts for the OER [12]. Herewith, we investigate a fast and direct synthetic route to grow B-C-N layers with enhanced electrocatalytic activity for the OER in alkaline aqueous solutions. The growth method is based on plasma-enhanced chemical vapour deposition (PE-CVD hereafter) using Methylamine Borane as a single-source precursor. This synthetic route has recently been proved to be efficient to grow BCNs on Cu substrates, achieving ultrathin layers formed by C-rich and h-BN-rich nanodomain patchworks that present high doping levels of B and N, and of C, respectively [13]. However, the electrochemical response of Cu substrates in alkaline solutions is quite complex, thus obscuring the analysis of the electrochemical behaviour of the BCNs, due to the unavoidable presence of pinholes in the obtained layers. Therefore, we chose Ti as an adequate substrate to grow B-C-N layers, since the electrochemical response of Ti for the OER in alkaline aqueous solutions is very weak. Moreover, Ti has a low work function value ( $\sim 4.33$  eV for polycrystalline samples) with respect to Cu ( $\sim 4.94$  eV for the (111) surface dominant in polycrystalline samples) [14], which facilitates the electronic transfer with the layers, thus diminishing the contact potential that could affect electrochemical measurements.

The obtained B-C-N layers grown on Ti have been first characterised with scanning electron microscopy (SEM), Raman spectroscopy, x-ray photoelectron spectroscopy (XPS) and transmission electron microscopy (TEM) coupled with electron energy loss spectroscopy (EELS). Next, electro-catalytic properties of the obtained layers for the OER have been investigated in alkaline aqueous solutions. Interestingly, it has been observed that the topmost surface of the Ti substrate presents an amorphous  $\text{TiO}_x$  layer, where the B-C-N layers are grown. This oxide layer shows photocatalytic activity for water splitting, which is preserved by the B-C-N layers grown on top. The spectral photo-electrochemical response of these layers has been analysed to determine the bandgap energy of the samples. Finally, electrochemical impedance spectroscopy measurements allowed us to obtain the flat band potential and establish the position of the band energy levels of the samples relative to oxidation and reduction potentials of water.

## 2. Experimental Methods

The growth of B-C-N layers on Ti substrates has been investigated by using two different synthetic methods: conventional and plasma-enhanced (or microwave-assisted) chemical vapour deposition (CVD and PE-CVD, respectively). We have followed the same growth methods previously used to grow B-C-N layers on Cu foil substrates. Ti (Goodfellow, 99.5%, 1 mm of thickness) substrates were cleaned in a mixture of 4% wt. HF + 30% wt. HNO<sub>3</sub> for 30 seconds, rinsed in deionized water and dried in air prior to the growth processes. A single-source molecular precursor containing B, C and N atoms, namely methylamine borane (BH<sub>3</sub>NH<sub>2</sub>CH<sub>3</sub>, MeAB hereafter), has been used, as in our previous works. Further details of the synthetic routes followed in CVD [15] and PE-CVD can be found elsewhere [13].

The morphology of the obtained layers has been analyzed by Scanning Electron Microscopy (SEM) in a Hitachi S3000 instrument. In addition, these have been characterized by Raman spectroscopy in a WITec ALPHA 300AR instrument using a confocal microscope with different lenses (20x and 100x). A laser with excitation wavelength of 532.3 nm and a power of 2 mW has been used.

The samples surface composition has been characterized by X-ray Photoelectron Spectroscopy (XPS) measurements, taken out in an Ultra High Vacuum (UHV) chamber, with a base pressure in the low 10<sup>-10</sup> mbar range. Photoelectrons, excited by a MgK<sub>α</sub> photon source ( $h\nu = 1253.6$  eV), were measured with a hemispherical electron analyser (VG Microtech Clam-2) in constant pass energy (PE) mode set at 100 eV (energy resolution of 1 eV), further details are available in [13,15-17]. The binding energy (BE) was calibrated by acquiring after each measurement the Au 4f<sub>7/2</sub> core-level set at 84.0 eV BE. The PE-CVD-samples grown on Ti were air-transferred and mounted in the XPS ultra-high-vacuum system. The samples have been measured in the as received state as well as after annealing at 500 °C in UHV.

Transmission Electron Microscopy (TEM) images of the samples have been recorded in a JEM ARM 200F apparatus. In order to prevent decomposition of TiC<sub>x</sub>N<sub>y</sub> phases present in the samples, electron beam energy was fixed at 80 kV. Moreover, Electron Energy Loss Spectroscopy (EELS) and Scanning Transmission Electron Microscopy (STEM) analyses have been performed in the same apparatus. Samples have been transferred by scrapping the

layers (grown on the Ti substrates) with a scalpel onto the Cu grids of the TEM. The microscopic flakes transferred onto the TEM grids were analysed by optical microscopy coupled with confocal Raman spectroscopy prior to TEM measurements.

Electrochemical measurements were done in a three-electrode cell with 0.1 M KOH and 1 M KOH aqueous solutions as electrolytes. B-C-N layers grown on Ti substrates were used as working electrodes (WE), a platinum sheet with a geometric surface area of 9.0 cm<sup>2</sup> was the counter electrode (CE) and the reference electrode (RE) was a Ag/AgCl electrode filled with 1M KNO<sub>3</sub> solution (XR440 from Radiometer Analytical), having an electrode potential  $E_{Ag/AgCl}^0 = 484$  mV versus the Normal Hydrogen Electrode (NHE). Electrode potentials have been also converted to the Reversible Hydrogen Electrode (RHE) scale, due to the fact that the equilibrium potential for the OER has a fixed value (1.23 V) in this scale. The following equations have been used:

$$E_{NHE} = E_{Ag/AgCl} + E_{Ag/AgCl}^0 \quad (1a)$$

$$E_{RHE} = E_{Ag/AgCl} + E_{Ag/AgCl}^0 + 0.059 \cdot pH \quad (1b)$$

Where  $E_{Ag/AgCl}$  is the experimentally determined electrode potential (vs. the RE used here),  $E_{NHE}$  is the electrode potential in the NHE scale,  $E_{RHE}$  is the electrode potential in the RHE scale and pH is the pH of the solution (pH=13.0 and 13.7 for 0.1M and 1M KOH solutions, respectively).

Due to the design of the WE holder, the geometric electrode area in contact with the electrolyte and under illumination was of 1.13 cm<sup>2</sup>. Current density at fixed electrode potential, linear sweep voltammetry (LSV) curves (at dark and under illumination), cyclic voltammetry runs (CV) and impedance through the WE/electrolyte junction as a function of the bias potential were measured with a potentiostat-galvanostat PGSTAT302N (Autolab) provided with an integrated impedance module FRAIL. AC modulated cyclic voltage scans of 10 mV amplitude in the 100 to 1000 Hz frequency range at different electrode potentials ranging from -2.0 V to 1.0 V (vs. NHE) were used.

A Xe lamp (Jobin Yvon) of 75 W was used as visible-UV light source. A quadrupole mass spectrometer (QMS, Mod. Prisma, Balzers) coupled to the photo-electrochemical cell was used to analyse the qualitative composition of the gases evolved from the cell. During

electrochemical measurements, Argon was bubbled through the electrolyte at a constant flow of 28.8 sccm. Further details of the experimental system are reported in [18-20] and in the SI (Figure S7).

### 3. Results and discussion

#### 3.1. Morphological and structural characterization of the B-C-N layers

We first investigated B-C-N on Ti grown by conventional CVD, by following the same method previously used to grow B-C-N layers on Cu foil substrates [15]. The typical surface morphology obtained (SEM image in Figure 1a) shows polyhedral-shaped crystals. Raman spectroscopy shows three bands at 250, 441 and 611  $\text{cm}^{-1}$  (Figure 1d), characteristic of rutile- $\text{TiO}_2$  [19]. The formation of  $\text{TiO}_2$  is due to the strong affinity of Titanium for Oxygen, as Ti is usually employed as a getter for  $\text{O}_2$ . Several attempts were done by varying the CVD reactor conditions and temperature of the Ti substrate (from 1000  $^{\circ}\text{C}$  down to 800  $^{\circ}\text{C}$ ), but rutile- $\text{TiO}_2$  was the only phase observed on the surface in all cases. Furthermore, the typical Raman bands associated to B-C-N are negligible. Thus, the CVD growth of B-C-N layers is quenched by surface oxidation of Ti.

On the contrary, the use of PE-CVD allows a fast and continuous growth of B-C-N layers on Ti, as unveiled by the appearance of the typical D and G Raman bands characteristic of  $\text{sp}^2$ -hybridized C [22-24] and B-C-N layers [13,15,17,25] at 1350 and 1590  $\text{cm}^{-1}$  (Figure 1e), respectively. By using Ti disks substrates, fusion was not observed, owing to the high fusion temperature of Ti, as well as to the high thickness (1 mm) of the Ti substrates, as compared to the Cu substrates previously used (25  $\mu\text{m}$ ) [13]. However, growth time has a clear effect both in the morphology (Figure 1b,c) and in the composition of the obtained layers. Samples obtained using low growth times (5 s), referred as Ti-BCN hereafter, show the same morphology of the pristine Ti surface (Figure 1b), suggesting the formation of very thin B-C-N flat layers, as it occurs when using Cu substrates for PE-CVD growth [13]. On the other hand, samples obtained using longer growth times (10 s), named TiCN-BCN hereafter, present a rougher surface morphology (Figure 1c and Figure S1 in the SI). This morphology suggests the growth of vertical wall structures, which are typically observed in graphene samples grown by PE-CVD. According to previous works, flat layers are initially formed during PE-CVD growth, whereas vertical wall flakes appear when using longer growth times

[26,27], in agreement with the morphologies obtained in the present B-C-N samples obtained with different growth times.

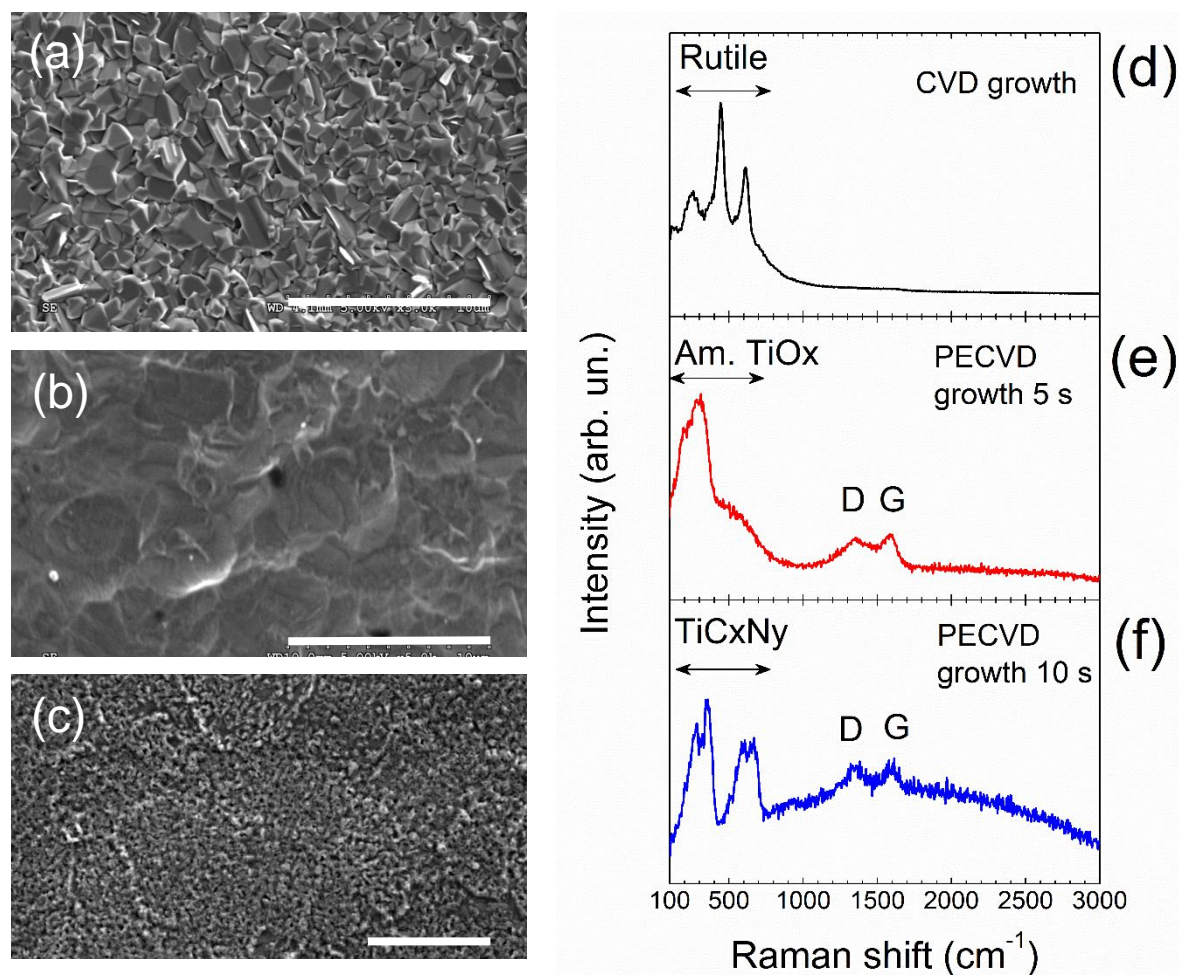


**Figure 1.** Scanning electron micrographs of: (a) sample obtained by CVD growth; (b) sample obtained by PE-CVD growth during 5 s (named Ti-BCN); (c) sample obtained by PECVD growth during 10 s (named TiCN-BCN). Scale bar is 10 μm in all cases. (d-f) Corresponding Raman spectra of the three samples.

The D and G Raman bands, characteristic of  $sp^2$ -hybridized B-C-N layers are present for both PE-CVD grown samples, independent on growth time, hence on surface morphology. Their relative intensity ratio is a hint of a high defect density [28], and their width suggests a poorly crystalline nature of the B-C-N layer, with possibly a non-homogeneous chemical



composition. For the short-time sample (Ti-BCN), an additional broad band around  $290\text{ cm}^{-1}$ , with two broad shoulders at  $195$  and  $515\text{ cm}^{-1}$  is also present in the Raman spectrum (see Figure 1e). These Raman signatures are ascribed to the presence of an amorphous  $\text{TiO}_x$  layer [29-33], which seems to be formed due to residual oxygen species present in the ampoules used for PE-CVD growth. Indeed, the Raman spectrum of a similar sample obtained by PE-CVD without using MeAB precursor (creating a plasma with the residual vacuum contained in the ampoule) presents similar Raman bands, as it can be seen in the SI (Figure S2). Further confirmation of the presence of  $\text{TiO}_x$  species at the surface of Ti-BCN samples have been obtained based on XPS measurements, as it will be shown later.

The Raman spectrum of a typical sample obtained by using a growth time of  $10\text{ s}$  (TiCN-BCN), besides the broad D and G bands of the B-C-N layers, presents four additional peaks at about  $285$ ,  $355$ ,  $600$  and  $660\text{ cm}^{-1}$  (see Figure 1f). These peaks suggest formation of titanium carbonitride phases ( $\text{TiC}_x\text{N}_y$ ) [34,35], due to the longer PE-CVD growth time and the subsequent higher temperatures achieved.

These results point out the enhanced versatility of the PE-CVD method as compared to conventional CVD process to efficiently grow B-C-N layers on Ti substrates. Whereas CVD is not suitable to grow B-C-N layers on Ti, PE-CVD allows the formation of different structures on Ti depending on the growth conditions. In conventional CVD growth, the molecular species giving rise to the formation of the B-C-N layers are the products of the thermolytic decomposition of the molecular precursor [15] (in this work MeAB). Since these molecular species have a lower reactivity with the Ti substrate than the residual Oxygen species present in the reactor, a rutile- $\text{TiO}_2$  phase is formed. On the contrary, the PE-CVD route produces the formation of free radicals and ion species, which are much more reactive with the Ti substrates than the neutral molecules formed by MeAB thermolysis. This implies a much faster growth mechanism, giving rise to the successful synthesis of B-C-N layers on top of the Ti substrates. This result is similar to that observed for the growth of graphene on catalytically inert substrates. In fact, PE-CVD methods are suitable to grow graphene on such a type of substrates, for instance on h-BN [36] or glass [37], where conventional CVD methods are usually unsuccessful or require very long growth times [38].

### 3.2. Surface chemical composition and element distribution

Once investigated the differences in morphology and vibrational bands for the B-C-N layers grown on Ti with the two different growth times, we carry out a further characterization by XPS, to enlighten the surface stoichiometry and element chemical bonding state. The B, C, N 1s and the Ti 2p core-levels for both the Ti-BCN and TiCN-BCN samples, along with the results of a fitting analysis of the different components, are shown in Figure 2. Samples have been annealed to 500 °C after insertion in UHV, to get rid of ambient surface contamination (survey spectra and data of the pristine samples before vacuum annealing are reported in the SI, Figure S3 and Figure S4).

At a first sight (Figure 2), in both samples all spectral features appear with a large width and composed by more than one peak, suggesting the presence of different components, associated to the mutual bonding among the elements. Thus, a fitting analysis has been performed by using pseudo-Voigt line-shapes (Gaussian and Lorentz combination, representing the experimental uncertainty and the intrinsic excitation line-shape for each core level, respectively), after subtraction of a Shirley background, whose fitting parameters are reported in Tables S1 and S2 in the SI (Ti 2p spin-orbit splitting and intensity ratio are kept fixed). The single and sum fitting curves are plotted along with the experimental data and reported in Figure 2.

The B 1s core level in Ti-BCN (TiCN-BCN) presents two components, due to B-C and B-N bonds at 190.0 eV (190.1 eV) and 190.9 eV (191.0 eV) binding energy (BE), respectively [13,15,25,39,40], and a broader peak at 192.8 eV (192.3 eV) associated to multi-component coordination of B with oxygen [13,15,17,41], more intense for the Ti-BCN sample than for the TiCN-BCN one (in accord with the more intense O contamination of Ti-BCN in the survey spectra shown in Fig. S3 of the SI). In the C 1s core-level, four main components emerge, due to the C-C bonding at 284.8 eV typical signature of sp<sup>2</sup>-bonded carbon, the C-N bonding at 285.5 eV (285.4 eV), and the C-B one at 283.8 eV (283.6 eV) [13,15,25,39,40]; a latter broader feature at higher BE takes into account the C-to-oxygen contamination. There is a lower BE peak (282.1 eV) in the TiCN-BCN sample, signature of Ti-C bonding [42], which is absent in the Ti-BCN sample. The N 1s core-level is characterized by the more intense lower BE component due to N-B bonds, at 398.2 eV (398.5 eV), signature of the

hexagonal planar B-N bonding for both samples, and the N-C bonding at 399.0 eV (398.9 eV) [13,15,25,39,40]. In the TiCN-BCN sample a further peak at 397.1 eV BE indicates the presence of Ti-N bonding [42].

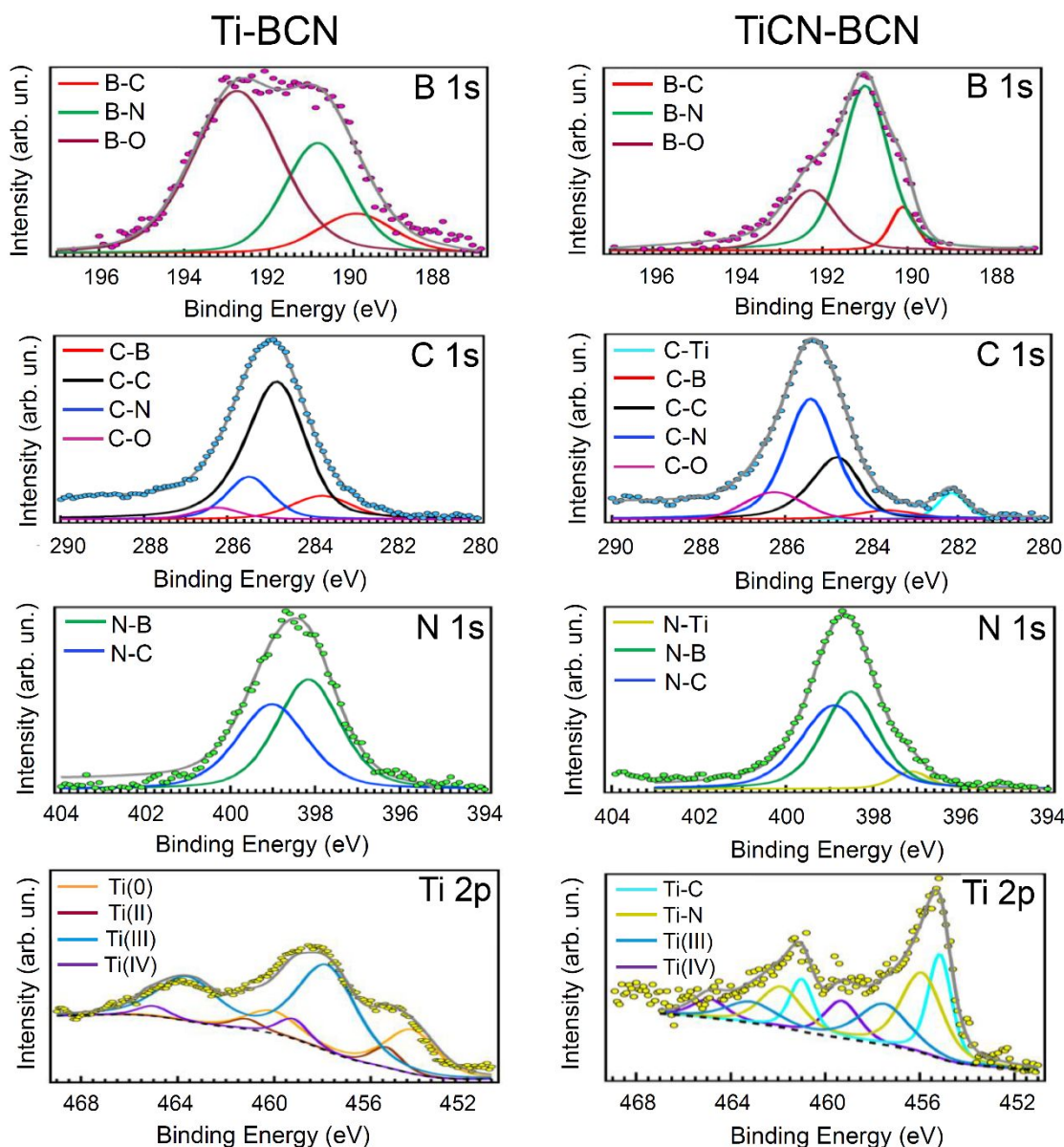


**Figure 2.** XPS core-level data of the Ti-BCN (left panels) and of the TiCN-BCN samples (right panels), both after 500 °C annealing. From the top to the bottom: B 1s, C 1s, N 1s, Ti 2p core levels; experimental data (dots), Shirley background (dashed lines) fitting curve (grey continuous line) and single fitting components (coloured lines), as described in the legends of the figures.

Thus, the B, C and N 1s core-levels present the typical features associated to mutual chemically interacting  $sp^2$ -bonded elements. This is a clear signature of formation of ternary B-C-N planar layers in both samples, constituted by heavily C-doped h-BN and heavily B and N doped graphene, whose intensity ratio estimated taking into account the photo-excitation cross-section [43] results as B:C:N = 0.3:1.0:0.4 for Ti-BCN and 0.6:1.0:0.9 for TiCN-BCN.

On the other hand, the Ti 2p core-levels whose signal comes from the substrate, present a different surface chemical status for the two samples. There are several Ti components for the Ti-BCN sample coming from the substrate, from metallic Ti (2p<sub>3/2</sub> at 454.0 eV BE), to Ti (II), Ti(III) and Ti(IV) components characteristic of TiO, Ti<sub>2</sub>O<sub>3</sub>, TiO<sub>2</sub> [44] present at the Ti surface for the Ti-BCN sample. At the TiCN-BCN sample, Ti peaks are observed associated to Ti-N and Ti-C bonds [42], and to Ti<sub>2</sub>O<sub>3</sub> and TiO<sub>2</sub> oxides [44]. Hence, several coordinated TiO<sub>x</sub> thin surface oxides are formed by short-time PE-CVD exposition, while surface TiC<sub>x</sub>N<sub>y</sub> is also produced for longer exposure times.

Additional evidences of the formation of TiC<sub>x</sub>N<sub>y</sub> phases are obtained by XRD (see Figure S5 in the SI) and TEM (Figure 3). The TEM image of the TiCN-BCN sample in Figure 3a shows a poorly-crystalline / amorphous structure. At higher spatial resolution, two distinct regions can be appreciated (Figure 3b): the outer region (marked as 1 in the image) with a thickness of about 7 nm and an amorphous structure, presents an EELS spectrum (Figure 3d) indicating the formation of B, C and N atoms arranged in a  $sp^2$ -hybridization (evidenced by the observation of  $\pi^*$  and  $\sigma^*$  transitions), with small traces of O; the inner region (marked as 2 in Figure 3b) contains Ti in addition to B, C and N (EELS in Figure 3e).

A spatial mapping of the four elements recorded by EELS (in the yellow region marked in Figure 3c) is reported in Figure 3g, evidencing a core/shell structure. On the other hand, well-resolved EELS spectra of B, C, N and Ti in the inner region (region 2 in Figure 3b) are shown in Figure 3f. Peak energy maxima of B, C, N and Ti EELS features in both regions (regions 1 and 2 in Figure 3b) are listed in Table S3 (see the SI). EELS peak positions of B, C and N K-edge absorption in the outer layer (region 1 in Figure 3b) are in good agreement with those previously reported for h-BN, graphitic carbon and  $sp^2$ -hybridized B-C-N layers (see Table S3 in the SI and references therein). This indicates that the outer shell is formed by a

graphitic-like layer of B-C-N. Whereas B peak remains unchanged, shifts in peak positions of C and N K-edges are observed when comparing EEL spectra acquired in the outer shell and in the inner core. This indicates that an additional phase is present in that inner region, below the B-C-N outer shell. The position of Ti  $L_{2,3}$  peak (see Table S3 in the SI) confirms that this phase consists in Ti carbonitride. Therefore, TEM results reveal the formation of a core/shell structure composed by an inner  $\text{TiC}_x\text{N}_y$  core surrounded by an outer B-C-N layer, in good accordance with Raman, XPS and XRD results.

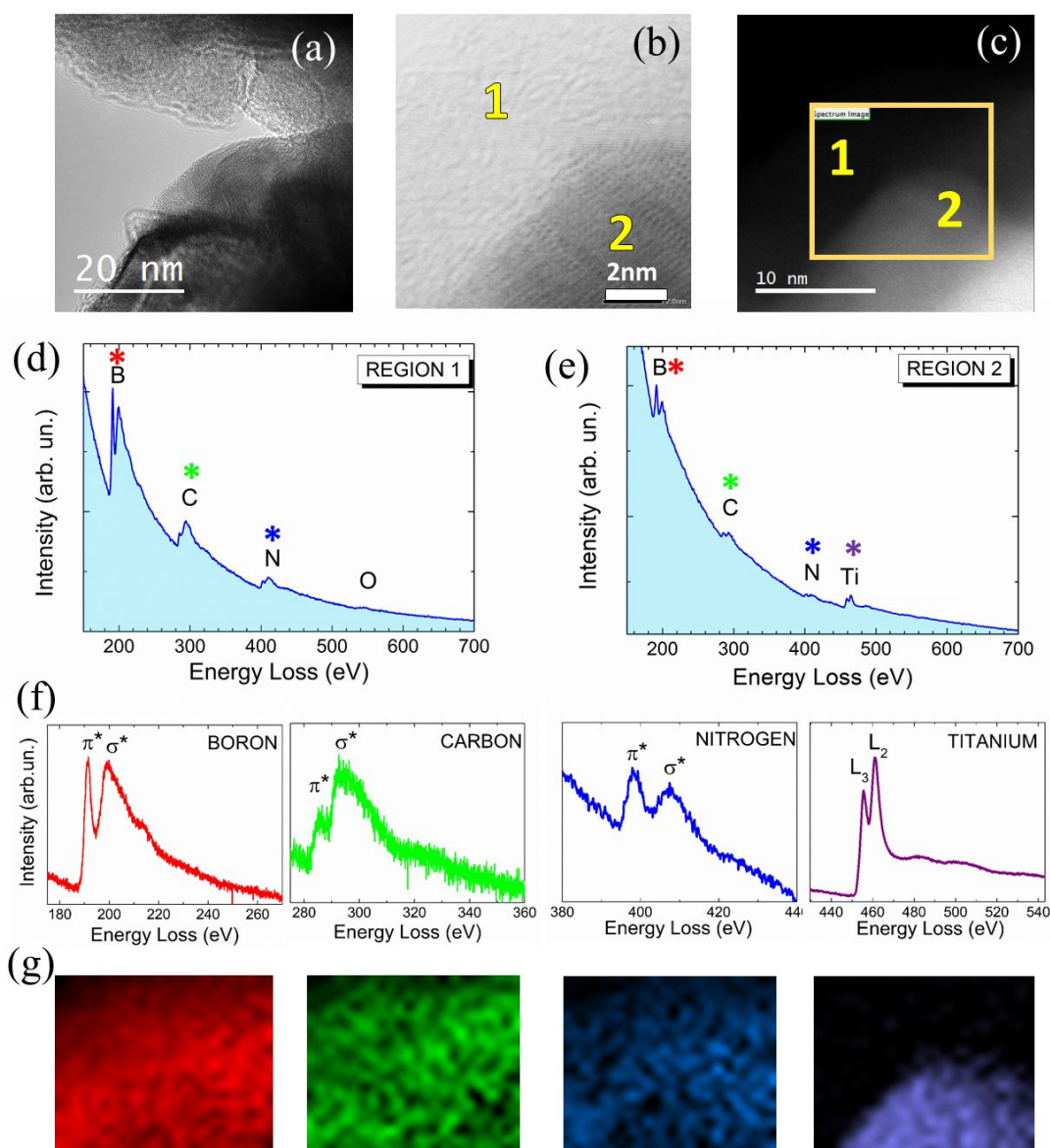


**Figure 3.** (a) TEM image of TiCN-BCN sample; (b) HRTEM bright-field image showing two clearly distinct regions (marked as 1 and 2); (c) Image of the same zone obtained in

STEM mode; (d) EELS data acquired in region 1, showing K-edge absorption signals of B, C and N as well as a weak O signal; (e) EELS data acquired in region 2, showing K-edge absorption signals of B, C and N as well as  $L_{2,3}$  absorption peak of Ti; (f) well-resolved B, C, N and Ti EELS peaks in region 2; (g) mapping of B (red), C (green), N (blue) and Ti (violet) obtained in STEM mode in the region marked by a yellow rectangle in Figure 3c.

### 3.3. Electrocatalytic activity for the OER

Electrocatalytic activities of the samples for the OER have been investigated by recording Linear Sweep Voltammetry (LSV) curves. Figure 4a shows the comparison of electrolytic current densities (calculated by using the geometric surface area of the electrodes) as a function of the applied electrode potential for different samples. LSV curve of a Pt disk is also shown for comparison purposes. The bare Ti disk substrate presents weak electrolytic currents even at high potential values, showing poor electrocatalytic activity for the OER. The growth of a B-C-N layer on top of the Ti substrate (Ti-BCN sample) produces an enormous increase (about 60-fold at  $E=1.8$  V vs. RHE) in the electrolytic current. This increase is even higher for the TiCN-BCN sample (about 170-fold increase at  $E=1.8$  V vs. RHE as compared to the bare Ti substrate). The higher electrolytic currents observed in TiCN-BCN samples as compared to Ti-BCN ones may be ascribed to differences in sample morphology rather than in surface composition. In fact, according to the above characterizations, the surface topmost layers (which are responsible of the electrocatalytic activity) are similar in both sets of samples, formed by a heterogeneous B-C-N layer in both cases. Moreover, the LSV curve of TiCN-BCN is approximately 3 times higher than that of Ti-BCN one over the entire electrode potential range, suggesting that the former sample has a real surface area 3 times larger than the later one. This is also in qualitative agreement with the surface morphologies observed by SEM (Figures 1b,c and Figure S1 in the SI). It must be noticed that Pt presents better electrocatalytic activity as compared to Ti-BCN and TiCN-BCN samples, but the overpotential for the onset of the OER of Ti-BCN and TiCN-BCN samples are similar to that of Pt (of about 0.4 V). These overpotential values are comparable to those usually observed in other electrode materials used for the OER [45,46].



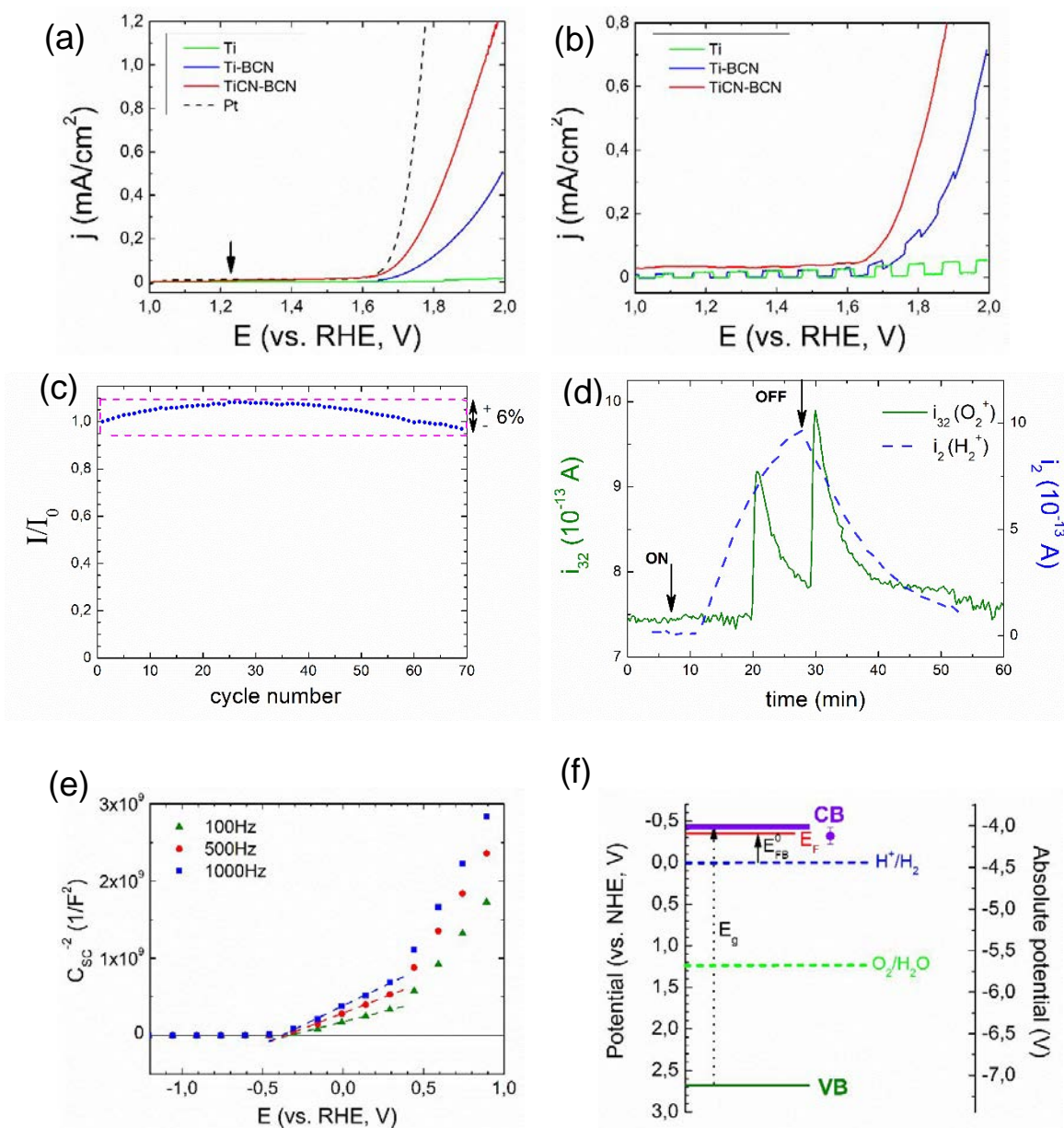


**Figure 4.** Linear sweep voltammetry curves of Ti-BCN, TiCN-BCN, Ti substrate and Pt recorded at a scan rate of  $10 \text{ mV s}^{-1}$  in 1M KOH electrolyte in (a) dark conditions and (b) under intermittent illumination conditions; (c) evolution of the electrolytic current recorded at 2 V (vs. RHE) with cycle number obtained during consecutive CV runs taken in the 1-2 V (vs. RHE) range at  $5 \text{ mV/s}$ ; (d) time evolution of the mass spectrometric ionic currents related to  $O_2$  ( $i_{32}$ ) and  $H_2$  ( $i_2$ ) species, recorded during water electrolysis using a Ti-BCN anode in 1M KOH aqueous solution. The arrows indicate the start and stop of the electrolysis at a fixed electrode current of 2 mA. (e) Mott-Schottky plot of the space charge layer capacitance ( $C_{sc}$ ) as a function of the applied electrode potential; (f) schematic representation of the

positions of the valence and conduction bands (VB and CB, respectively) and the Fermi level ( $E_F$ ) of Ti-BCN electrodes relative to water oxidation/reduction potentials. The violet point indicates the position of CB calculated using equation (4).

Cycling stability of Ti-BCN electrodes has been investigated by CV measurements recorded in the 1-2 V (vs. RHE) range at 5 mV/s. In Figure 4c the evolution of the electrolytic current at 2 V (vs. RHE) obtained during consecutive CV runs is plotted as a function of cycle number, normalized to the current recorded during the first cycle ( $I_0$ ). Relative variations in the electrolytic current recorded in CV curves lie within  $\pm 6\%$  over 70 cycles, thus demonstrating a good electrode stability. It is worth to mention that the charge passed through the electrode during each CV run (which can be obtained by time integration of the electrolytic current, being about 30 mC) is higher than the charge necessary to oxidize the electrode itself (which can be estimated assuming a  $B_xC_yN_z$  layer with a thickness of 4 nm and an electrode area in contact with the electrolyte of 1.13 cm<sup>2</sup>). Therefore, the good electrode stability observed in Figure 4c indicates that the oxidation of the atoms forming the electrode itself is negligible and the electrolytic current is due to water oxidation with a high Faradaic efficiency.

The amounts of H<sub>2</sub> and O<sub>2</sub> evolved during electrolysis in 1M KOH electrolyte using a Ti-BCN electrode have been determined by mass spectrometric analyses of the evolved gases. Further details on the experimental setup for gas analysis and of the calibration measurements done for quantitative analysis can be found in Figures S8-S10 in the SI. The time evolution of  $i_2$  and  $i_{32}$  mass spectrometric ionic currents (which are proportional to the H<sub>2</sub> and O<sub>2</sub> flows, respectively) recorded at a fixed electrolytic current of 2 mA is shown in Figure 4d. Due to the high volume of the photo-electrolytic cell (of about 350 ml), there is a dwell time between the start of the electrolysis and the detection of gases at the QMS, related to the transport of gases from the electrodes to the QMS. Whereas small H<sub>2</sub> bubbles evolved continuously from the Pt cathode, the flatness of the Ti-BCN anode gave rise to the formation of large oxygen bubbles. These bubbles gradually increased in size until evolving (see Figure S11 in the SI), thus giving rise to two peaks in the  $i_{32}$  signal, instead of a continuous increase in the  $i_{32}$  signal. It must be noticed that the electrolytic current was switched off just after the release of the



second O<sub>2</sub> bubble evolved at the electrode, thus ensuring that most of the generated O<sub>2</sub> was detected. The H<sub>2</sub> and O<sub>2</sub> amounts determined by integration of  $i_2$  and  $i_{32}$  ionic currents (after background subtraction) and taking into account their respective detection sensitivities are equal to  $1.3 \cdot 10^{-5}$  mol and  $6.5(7) \cdot 10^{-6}$  mol, respectively. These values must be compared to those calculated by the total charge passed through the electrodes, namely  $1.305 \cdot 10^{-5}$  mol and  $6.53 \cdot 10^{-6}$  mol. The obtained results indicate that the Faradaic efficiencies of the HER and OER reactions occurring at the Pt and Ti-BCN electrodes, respectively, are close to 100%, within a 10% of experimental uncertainty. This result confirms that the oxidation of the Ti-BCN electrode is negligible, as deduced from the good electrode stability observed in cycling experiments (Figure 4c).

All these results point out the good electrocatalytic activities of the present samples for the OER. These electrocatalytic properties may be related to the heteroatom bonding scheme in the B-C-N layers. Although there are numerous studies on the electrocatalytic activity of graphene in different processes, it has been recently reported that pure and high-quality graphene layers are poor electrocatalysts and surface catalytically active sites are due to impurities [47] or defects [48]. Therefore, the high heteroatom doping by B and N of C-rich nanodomains obtained by PE-CVD growth in the present layers may be responsible of the improved electrocatalytic activity for the OER.

In addition to the interesting electrocatalytic properties of the present B-C-N layers, their ultrathin nature provides additional functionalities that can be exploited in photo-electrochemical water splitting applications. The photo-electrochemical response of the samples has been investigated by LSV under intermittent illumination (using a chopper between the light source and the electrode), as it can be seen in Figure 4b. The electrochemical current increases during illumination periods both for Ti disks and for Ti-BCN samples, whereas it remains essentially constant for TiCN-BCN. The absence of photoelectrochemical response in the TiCN-BCN samples seems to be due to the fact that the TiC<sub>x</sub>N<sub>y</sub> inner layer present in these samples has a metallic character and thus possesses a very low transmittance for the incident light and does not have an optical bandgap. On the other hand, the magnitude of the photocurrent (*i.e.*, the difference between electrochemical currents recorded under illumination and dark conditions) is similar in bare Ti substrates and in Ti-

BCN samples. The photocatalytic activity is therefore ascribed to the presence of a  $\text{TiO}_x$  layer on the surface of the samples, as observed by Raman and XPS analyses in the Ti-BCN sample, as well as by Raman analyses of bare Ti substrates recorded after photoelectrochemical tests (see Figure S6 in the SI). This in turn indicates that the B-C-N layers grown on the  $\text{TiO}_x$  surface are essentially transparent to light. Indeed, similar B-C-N layers grown on Cu substrates and subsequently transferred to transparent quartz substrates presented weak UV-vis absorption, having optical densities below 0.02 (or transmittances higher than 98%) in the 190-860 nm range [13]. Thus, the incident light goes through the B-C-N layers and creates electron/hole pairs in the  $\text{TiO}_x$  inner core. Holes cross the surface B-C-N layers and act as electron acceptors at the electrode/electrolyte interface. As a consequence, the ultrathin B-C-N layers grown on top of the  $\text{TiO}_x$  layer act as transparent electrodes with high conductivity for the photogenerated charge carriers and improved electrocatalytic activity for the oxidation of water to oxygen gas.

The photocurrents recorded at fixed electrode potential are quite stable, as shown in Figure S12 in the SI. It can be seen that the electrochemical current increases when the WE is illuminated by the Xe lamp (i.e., the photocurrent has positive values), which implies that the electrode presents a n-type behaviour. This n-type character is further confirmed by the sign of the open circuit voltage change recorded during illumination of the electrodes (see Figure S14 in the SI) and is in agreement with the n-type behaviour reported in  $\text{TiO}_2$  [49]. The spectral dependence of the photocurrent has been investigated by using optical filters, which allow determining the band gap of the inner  $\text{TiO}_x$  layer. The dependence of the photocurrent as a function of the maximum energy of incident photons can be seen in Figure S13 in the SI. It can be seen that photocurrents are observed only for photon energies higher than 3.1(2) eV, thus indicating that this is the band gap energy ( $E_g$ ) of the  $\text{TiO}_x$  layer. This value is in good accordance with reported band gaps of several titanium oxides, such as TiO,  $\text{Ti}_2\text{O}_3$  and  $\text{TiO}_2$  [50].

In order to characterize the interface of the Ti-BCN samples and the electrolyte, electrochemical impedance spectroscopy (EIS) measurements have been done. These measurements allow to determine the flat band potential ( $E_{FB}$ ), that is the potential that must be applied to the electrode to achieve flat bands over the electrode-electrolyte interface.  $E_{FB}$

has been determined from the space charge layer capacitance,  $C_{sc}$ , which is in turn obtained from the imaginary part of the impedance ( $Z_{im}$ ) [18,20].  $Z_{im}$  has been measured by AC modulated cyclic voltage scans from  $-2.0$  V to  $1.0$  V (vs. NHE) at different frequencies in the frequency range from  $100$  Hz to  $1000$  Hz. Then, the relationship between  $C_{sc}$  and  $E_{FB}$  is given by the Mott-Schottky equation:

$$\frac{1}{C_{sc}^2} = \left( \frac{2}{\epsilon \epsilon_0 A^2 e N_D} \right) \left( E - E_{FB} - \frac{k_B T}{e} \right) \quad (2)$$

where  $\epsilon$  is the dielectric constant of the electrode,  $\epsilon_0$  is the permittivity of vacuum,  $A$  is the area of the electrode,  $e$  is the charge of the electron,  $N_D$  is the density of donors,  $E$  is the applied electrode potential,  $k_B$  is Boltzmann's constant and  $T$  is the absolute temperature. The term  $k_B T/e$  in equation (3) can be neglected because it is very low as compared to  $E - E_{FB}$ . Figure 4e shows the Mott-Schottky plot at three different representative frequencies. A flat band potential value of  $-0.34(2)$  V (vs. RHE) has been obtained, both in Ti-BCN samples (Figure 4e) and in bare Ti substrates (Figure S15 in the SI).  $E_{FB}$  depends on the pH of the solution in oxide semiconductors according to [51]:

$$E_{FB} = E_{FB}^0 - 0.059 \cdot pH \quad (3)$$

where  $E_{FB}^0$  is the flat band potential at  $pH=0$ . In order to compare flat band potentials obtained in different electrolytes,  $E_{FB}^0$  values must be considered. In practice,  $E_{FB}^0$  values referenced to the NHE scale are the same than  $E_{FB}$  values referenced to the RHE scale. In fact, the RHE scale is usually employed to fix  $E_{FB}$  values because pH dependence of the flat band potential of the oxide can be neglected (pH dependence for both the flat band potential of the oxide and RHE are  $59$  mV/pH).

Then  $E_{FB}$  can be also referenced to the vacuum level, by taking into account the relationship of the reference electrode potentials and the absolute electrode potential [52]. This can be used to find the position of the Fermi level ( $E_F$ ) with respect to the vacuum level. In n-type semiconductors, which is the case in the present samples, the Fermi level is close to the conduction band (CB). In fact, the difference between the CB energy level ( $E_{CB}$ ) and  $E_F$  lies between  $0.1$ - $0.4$  eV, depending on the conductivity of the oxide electrode [53] (that difference decreases by increasing the conductivity). In turn, the conductivity of the layer depends on the density of donors (the conductivity increases with  $N_D$ ). The density of donors

estimated from the slope of Mott-Schottky plots recorded at 1 kHz in the present  $\text{TiO}_x$  layers range between  $2 \cdot 10^{17}$ - $10^{18} \text{ cm}^{-3}$ , depending on the value of the dielectric constant used (we estimated that  $\epsilon$  values range between  $\epsilon = 55$  characteristic of anatase- $\text{TiO}_2$  [54] and  $\epsilon = 170$  characteristic of rutile- $\text{TiO}_2$  [55]). The estimated values for the density of donors are similar to these reported in several semiconductors, including  $\text{TiO}_2$  [56].

On the other hand, by using the bandgap value determined from the measurement of the spectral response of the photocurrents and photo-potentials (Figures S13 and S14 in the SI), the position of the valence band (VB) can be obtained. Figure 4f shows the position of the VB and CB energy levels of the present Ti-BCN samples with respect to the vacuum level, together with the energy positions of the reduction and oxidation potentials of water at pH=0.

An independent way to find the position of the CB level is by using the semiempirical relationship between  $E_{CB}$  and  $E_g$ , which has been proved to be valid both in bulk [53] and ultrathin film oxides [57]:

$$E_{CB}(V \text{ vs RHE}) = 1.23 - \frac{E_g}{2} \quad (4)$$

The position of the CB band level calculated using the  $E_g$  value obtained from the spectral dependence of the photocurrents and equation (4) is plotted in Figure 4f (violet dot). It can be seen that this CB level is in agreement with the value of  $E_{FB}$  obtained by EIS measurements.

According to Figure 4f, it is concluded that the position of  $\text{TiO}_x$  energy bands in Ti-BCN samples is suitable for water dissociation. This result is in agreement with the reported energy levels of  $\text{TiO}_2$  samples [58]. It must be emphasized that the growth of B-C-N layers on the surface of the Ti substrates does not change either the value of  $E_{fb}$  or the bandgap of  $\text{TiO}_x$  and thus does not alter the position of the VB and CB in this material. Therefore, the photochemical properties of  $\text{TiO}_x$  are not altered by growing the B-C-N layers on top. Instead of that, the B-C-N layers have a positive impact on the photo-electrochemical response of  $\text{TiO}_x$ , by improving the electrocatalytic activity of the electrodes for the OER, while preserving the photochemical properties. This result may open interesting possibilities for improving photo-electrochemical devices used for water splitting. Precious catalysts like Pt islands/nanoparticles are usually deposited on top of the photocatalysts like  $\text{TiO}_2$  to facilitate

the OER reaction. The present results demonstrate that ultrathin transparent B-C-N layers with good electrocatalytic properties for the OER can be easily grown on top of  $\text{TiO}_x$ . This may lead to a higher interface area with the electrolyte thus improving the overall OER reaction as compared to the use of small metal islands along with a significant reduction in the cost of raw materials.

#### 4. Conclusions

The growth of ultrathin B-C-N layers on Ti substrates has been investigated using different synthetic methods. Conventional CVD route at 800-1000 °C gives rise to the formation of a rutile- $\text{TiO}_2$  layer that impedes the growth of B-C-N layers on top. On the contrary, the use of plasma-enhanced CVD allows the formation of different B-C-N structures depending on the growth time. Planar B-C-N ultrathin layers have been obtained by this method for short time growth conditions. These layers are grown on top of a thin amorphous titanium oxide layer that is formed on the Ti substrate, due to the unavoidable presence of oxygen traces. Increasing growth time produces vertical wall core/shell structures formed by B-C-N and titanium carbonitride phases. The analysis of the chemical composition and bonding scheme of B-C-N layers by XPS characterizations revealed that these are formed by C and h-BN rich nanodomains with high doping levels of B and N and of C, respectively. This highly heterogeneous bonding scheme give rise to enhanced electrocatalytic properties of the obtained layers for the oxygen evolution reaction in alkaline aqueous solutions. Cycling stability tests and quantitative analyses of the evolved gases indicate that the Faradaic efficiency of these electrodes for the OER is close to 100 %. Moreover, it has been observed that the ultrathin B-C-N layers grown on titanium oxide layer act as transparent electrodes with high conductivity for the photogenerated charge carriers, thus preserving the photocurrents of the underlying titanium oxide layer, while improving the surface electrocatalytic activity for the oxidation of water to oxygen gas. The present results may have important applications in the development of metal-free photochemical water splitting devices.

## ASSOCIATED CONTENT

**Supporting Information.** Additional characterizations of the samples by Field Emission Gun images, Raman spectra, XPS analyses and X ray Diffraction, as well as photo-electrochemical measurements and mass spectrometric analyses of the evolved gases are available free of charge.

## AUTHOR INFORMATION

### Corresponding author

\* Fabrice Leardini, Departamento de Física de Materiales, Universidad Autónoma de Madrid, Cantoblanco, 28049, Madrid (Spain), phone: +34 914976422, email: [fabrice.lear dini@uam.es](mailto:fabrice.lear dini@uam.es)

### Author Contributions

The manuscript was written through contributions of all authors. All authors have given approval to the final version of the manuscript. ‡These authors contributed equally.

### Funding Sources

This work has been funded under RTI2018-099794-B-I00 grant of Spanish MICINN, and by PRIN Grant FERMAT (2017KFY7XF) of Italian MIUR.

## ACKNOWLEDGEMENT

Technical assistance from Mr. Fernando Moreno, SIdI and Segainvex Facilities at UAM is gratefully acknowledged.

## REFERENCES

- [1] Tang, J.; Durrant, J.R.; Klug, D.R., Mechanism of Photocatalytic Water Splitting in  $\text{TiO}_2$ . Reaction of Water with Photoholes, Importance of Charge Carrier Dynamics, and Evidence for Four-Hole Chemistry, *J. Am. Chem. Soc.*, **2008**, 130 (42), 13885–13891
- [2] Jamesh, M.-I.; Sun, X. Recent progress on earth abundant electrocatalysts for oxygen evolution reaction (OER) in alkaline medium to achieve efficient water splitting – A Review, *Journal of Power Sources*, **2018**, 400, 31-68
- [3] Antonietti, M.; Savateev, A.; Splitting Water by Electrochemistry and Artificial Photosynthesis: Excellent Science but a Nightmare of Translation? *Chem. Rec.* **2018**, 18, 969–972
- [4] Di, J.; Yan, C.; Handoko, A.D.; Seh, Z.W.; Li, H. Liu, Z. Ultrathin two-dimensional materials for photo- and electrocatalytic hydrogen evolution, *Materials Today* **2018**, 21 (7), 749-770
- [5] Chhetri, M.; Maitra, S.; Chakraborty, H.; Waghmareb, U.V.; Rao, C.N.R. Superior performance of borocarbonitrides,  $\text{BxCyNz}$ , as stable, low-cost metal-free electrocatalysts for the hydrogen evolution reaction, *Energy Environ. Sci.* **2016**, 9, 95
- [6] Rao C.N.R, Chhetri M. Borocarbonitrides as Metal-Free Catalysts for the Hydrogen Evolution Reaction, *Adv. Mater.* **2019**, 31, 1803668
- [7] Rao C.N.R, Gopalakrishnan K. Borocarbonitrides,  $\text{BxCyNz}$ : Synthesis, Characterization, and Properties with Potential Applications. *ACS Appl. Mater. Interfaces* **2017**, 9, 19478-19494
- [8] Rao C.N.R, Pramoda K. Borocarbonitrides,  $\text{BxCyNz}$ , 2D Nanocomposites with Novel Properties, *Bull. Chem. Soc. Japan* **2019**, 92, 441-468
- [9] Wang, S.; Zhang, L.; Xia, Z.; Roy, A.; Chang, D.W.; Baek, J.-B.; Dai, L. BCN Graphene as Efficient Metal-Free Electrocatalyst for the Oxygen Reduction Reaction, *Angew. Chem. Int. Ed.* **2012**, 51, 4209 –4212
- [10] Huang, C.; Chen, C.; Zhang, M.; Lin, L.; Ye, X.; Lin, S.; Antonietti, M.; Wang, X. Carbon-doped BN nanosheets for metal-free photoredox catalysis, *Nature Comm.* **2015**, 6:7698

- [11] Li, M.; Wang, Y.; Tang, P.; Xie, N.; Zhao, Y.; Liu, X.; Hu, G.; Xie, J.; Zhao, Y.; Tang, J.; Zhang, T.; Ma, D. Graphene with Atomic-Level In-Plane Decoration of h-BN Domains for Efficient Photocatalysis, *Chem. Mater.* **2017**, 29, 2769-2776
- [12] Balakrishnan, T.; Anis, M.; Arun, S.; Kumar, M.; Kumar, S.A.; Mayavan, S. BCN–Co<sub>3</sub>O<sub>4</sub> hybrid – a highly efficient catalyst for the oxygen evolution reaction and dye degradation, *RSC Adv.* **2016**, 6, 79448
- [13] Leardini, F.; Jiménez-Arévalo, N.; Ferrer, I.J.; Ares, J.R.; Molina, P.; Gómez Navarro, C.; Manzanares, Y.; Granados, D.; Urbanos, F.J.; García-García, F.J.; del Campo, A.; Avvisati, G.; Betti, M.G.; Mariani, C. A fast synthesis route of boron–carbon–nitrogen ultrathin layers towards highly mixed ternary B–C–N phases, *2D Mater.* **2019**, 6, 035015
- [14] CRC Handbook of Chemistry and Physics, 88th Edition, David R. Lide (editor), CRC Press (2007)
- [15] Leardini F.; Flores, E.; Galvis A.R.; Ferrer, I.J.; Ares, J.R.; Sánchez, C.; Molina, P.; C. van der Meulen, H.P.; Navarro, C.G.; Polin, G.L.; Urbanos, F.J.; Granados, D.; Garcia-Garcia, F.J.; Demirci, U.B.; Yot, P.G.; Mastrangelo, F.; Betti, M.G.; Mariani, C. Chemical vapor deposition growth of boron–carbon–nitrogen layers from methylamine borane thermolysis products *Nanotechnology* **2018**, 29 025603
- [16] Massimi, L.; Angelucci, M.; Gargiani, P.; Betti, M.G.; Montoro, S. Metal-phthalocyanine ordered layers on Au(110): metal-dependent adsorption energy *J. Chem. Phys.* **2014**, 140, 244704
- [17] Massimi L.; Betti M.G.; Caramazza S.; Postorino, P.; Mariani, C.; Latini, A.; Leardini, F. In-vacuum thermolysis of ethane 1,2-diamineborane for the synthesis of ternary borocarbonitrides *Nanotechnology* **2016**, 27, 435601
- [18] Barawi, M.; Flores, E.; Ferrer, I.J.; Ares, J.R.; Sánchez, C. Titanium trisulphide (TiS<sub>3</sub>) nanoribbons for easy hydrogen photogeneration under visible light, *J. Mater. Chem. A*, **2015**, 3, 7959
- [19] Barawi, M.; Ferrer, I.J.; Flores, E.; Yoda, S.; Ares, J.R.; Sánchez, C. Hydrogen Photoassisted Generation by Visible Light and an Earth Abundant Photocatalyst: Pyrite (FeS<sub>2</sub>), *J. Phys. Chem. C* **2016**, 120, 9547–9552

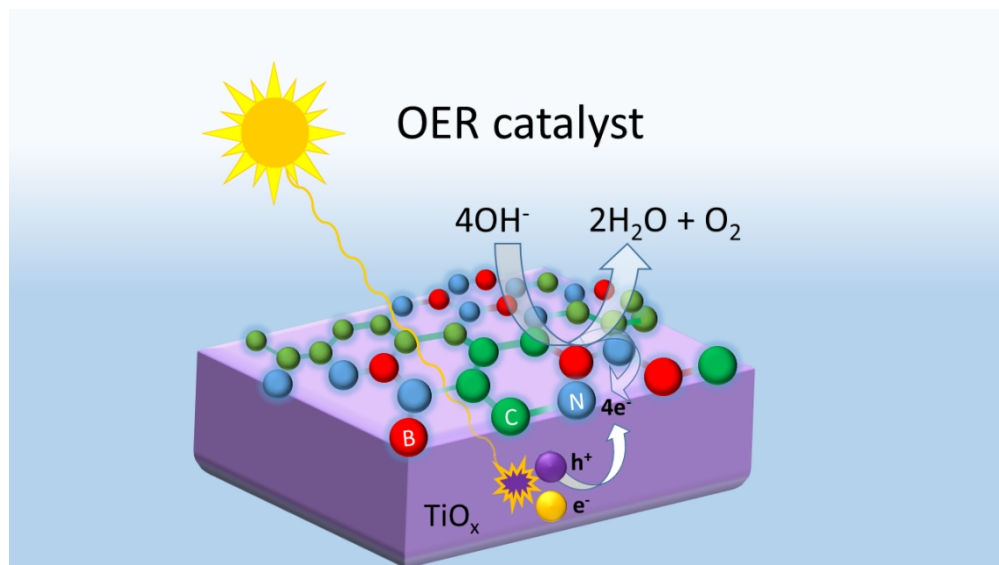


- [20] Flores, E.; Ares, J.R.; Sánchez, C.; Ferrer, I.J. Ternary transition titanium-niobium trisulfide as photoanode for assisted water splitting, *Catalysis Today* **2019**, 321–322, 107–112
- [21] Swamy, V.; Muddle, B.C.; Dai, Q. Size-dependent modifications of the Raman spectrum of rutile TiO<sub>2</sub>, *Appl. Phys. Lett.* **2006**, 89, 163118
- [22] Ferrari, A.C. Raman spectroscopy of graphene and graphite: disorder, electron–phonon coupling, doping and nonadiabatic effects. *Solid State Communications* **2007**, 143, 47–57.
- [23] Di Bernardo, I.; Avvisati, G.; Mariani, C.; Motta, N.; Chen, C.; Avila, J.; Asensio, M.C.; Lupi, S.; Ito, Y.; Chen, M.; Fujita, T.; Betti, M.G. Two-Dimensional Hallmark of Highly Interconnected Three-Dimensional Nanoporous Graphene, *ACS Omega* **2017**, 2, 3691–3697
- [24] Di Bernardo, I.; Avvisati, G.; Chen, C.; Avila, J.; Asensio, M.C.; Hu, K.; Ito, Y.; Hines, P.; Lipton-Duffin, J.; Rintoul, L.; Motta, N.; Mariani, C.; Betti, M.G. Topology and doping effects in three-dimensional nanoporous graphene, *Carbon* **2018**, 131, 258–265
- [25] Ci, L. ; Song, L.; Jin, C. ; Jariwala, D.; Wu, D. ; Li, Y. ; Srivastava, A.; Wang, Z.F.; Storr, K.; Balicas, L.; Liu, F.; Ajayan, P.M. Atomic layers of hybridized boron nitride and graphene domains, *Nat. Mater.* **2010**, 9 430–5
- [26] Sun, J.; Chen, Y.; Cai, X.; Ma, B.; Chen, Z.; Priyadarshi, M. K.; Chen, K.; Gao, T.; Song, X.; Ji, Q.; Guo, X.; Zou, D.; Zhang, Y.; Liu, Z. Direct low-temperature synthesis of graphene on various glasses by plasma-enhanced chemical vapor deposition for versatile, cost-effective electrodes, *Nano Res.* **2015**, 8, 3496
- [27] Ci, H.; Ren, H.; Qi, Y.; Chen, X.; Chen, Z.; Zhang, J.; Zhang, Y.; Liu, Z. 6-inch uniform vertically-oriented graphene on soda-lime glass for photothermal applications, *Nano Res.* **2018**, 11, 3106
- [28] Cançado, L.G.; Jorio, A.; Martins Ferreira, E.H.; Stavale, F.; Achete, C.A.; Capaz, R.B.; Moutinho, M.V.O.; Lombardo, A.; Kulmala, T.S.; Ferrari, A.C. Quantifying defects in graphene via Raman spectroscopy at different excitation energies. *Nano Letters* **2011**, 11, 3190–3196
- [29] Nemanich, R.; Tsai, C.; Connell, G. Interference-Enhanced Raman Scattering of Very Thin Titanium and Titanium Oxide Films” *Phys. Rev. Lett.* **1980**, 44, 273–276

- [28] Hsu, L.S.; Solanki, R.; Collins, G.J.; She, C.Y. Raman study of structural transformation of titania coatings induced by laser annealing, *Appl. Phys. Lett.* **1984**, 45, 1065-1067
- [30] Landis, E.C.; Philips, K.C.; Mazur, E.; Friend, C.M. Formation of nanostructured TiO<sub>2</sub> by femtosecond laser irradiation of titanium in O<sub>2</sub>, *J. Appl. Phys.* **2012**, 112, 063108
- [32] Lee, C.M.; Choi, J. Stoichiometry and structure driven optical properties of carbon incorporated titanium oxide thin films, *Optical Materials Express* **2016**, 6(11), 3594
- [33] Zimbone, M.; Cacciato, G.; Sanz, R.; Carles, R.; Gulino, A.; Privitera, V.; Grimaldi, M.G. Black TiO<sub>x</sub> photocatalyst obtained by laser irradiation in water, *Catalysis Communications* **2016**, 84, 11–15
- [34] Zheng, J.; Hao, J.; Liu, X.; Liu, W. Properties of TiN/TiCN multilayer films by direct current magnetron sputtering, *Journal of Physics D: Applied Physics* **2012**, 45, 095303.
- [35] Escobar-Alarcon, L.; Medina, V.; Camps, E.; Romero, S.; Fernandez, M.; Solis-Casados, M. Microstructural characterization of Ti–C–N thin films prepared by reactive crossed beam pulsed laser deposition. *Applied Surface Science* **2011**, 257, 9033-9037
- [36] Yang, W.; Chen, G.; Shi, Z.; Liu, C.-C.; Zhang, L.; Xie, G.; Cheng, M.; Wang, D.; Yang, R.; Shi, D.; Watanabe, K.; Taniguchi, T.; Yao, Y.; Zhang, Y.; Zhang, G. Epitaxial Growth of Single-domain Graphene on Hexagonal Boron Nitride. *Nat. Mater.* **2013**, 12, 792–797
- [37] Chen, Z.; Qi, Y.; Chen, X.; Zhang, Y.; Liu, Z. Direct CVD Growth of Graphene on Traditional Glass: Methods and Mechanisms, *Adv. Mater.* **2019**, 31, 1803639
- [38] Son, M.; Lim, H.; Hong, M.; Choi, H.C. Direct growth of graphene pad on exfoliated hexagonal boron nitride surface. *Nanoscale* **2011**, 3, 3089–93
- [39] Nappini, S.; Bondino, F.; Piš, I.; Chelleri, R.; Greco, S.L.; Lazzarino, M.; Magnano, E. Chemical composition and interaction strength of two-dimensional boron-nitrogen-carbon heterostructures driven by polycrystalline metallic surfaces, *Applied Surface Science* **2019**, 479, 903–913
- [40] Attri, R.; Sreedhara, M. B.; Rao, C. N. R. Compositional Tuning of Electrical and Optical Properties of PLD Generated Thin Films of 2D Borocarbonitrides (BN)<sub>1-x</sub>(C)<sub>x</sub>, *ACS Appl. Electron. Mater.* **2019**, 1, 569–576

- [41] Ong, C.W.; Huang, H.; Zheng, B.; Kwok, R.W.M.; Hui, V.; Lau, W.M. X-ray photoemission spectroscopy of nonmetallic materials: electronic structures of boron and  $B_xO_y$ , *J. Appl. Phys.* **2004**, 95, 3527
- [42] Restrepo Parra, E.; Arango Arango, P.J.; Benavides Palacio, V.J. XPS structure analysis of TiN/TiC bilayers produced by pulsed vacuum arc discharge, DYNA-COLOMBIA 2010, 77(163), 64-74, ISSN = {0012-7353}
- [43] Yeh, J.J.; Lindau, I. Atomic subshell photoionization cross sections and asymmetry parameters:  $1 \leq Z \leq 103$ . *At. Data Nucl. Data Tables* **1985**, 32, 1–155
- [44] Biesinger, M.C.; Lau, L.W.M.; Gerson, A.R.; Smart, R.St.C. Resolving surface chemical states in XPS analysis of first row transition metals, oxides and hydroxides: Sc, Ti, V, Cu and Zn, *Applied Surface Science* **2010**, 257 (3), 887-898
- [45] Eftekhari, A. Tuning the electrocatalysts for oxygen evolution reaction, *Materials Today Energy* **2017**, 5, 37-57
- [46] Merle, G.; Abrahams, I.; Barralet, J. Powerful amorphous mixed metal catalyst for efficient water-oxidation, *Materials Today Energy* **2018**, 9, 247-253
- [47] Mazánek, V.; Luxa, J.; Matějková, S.; Kučera, J.; Sedmidubský, D.; Pumera, M.; Sofer, Z. Ultrapure Graphene Is a Poor Electrocatalyst: Definitive Proof of the Key Role of Metallic Impurities in Graphene-Based Electrocatalysis, *ACS Nano* **2019**, 13, 1574–1582
- [48] Najafi, L.; Bellani, S.; Oropesa-Nuñez, R.; Martín-García, B.; Prato, M.; Bonaccorso, F. Single-/Few-Layer Graphene as Long-Lasting Electrocatalyst for Hydrogen Evolution Reaction, *ACS Appl. Energy Mater.* **2019**, 2, 5373–5379
- [49] Schneider, J.; Matsuoka, M.; Takeuchi, M.; Zhang, J.; Horiuchi, Y.; Anpo, M.; Bahnemann, D.W. Understanding  $TiO_2$  Photocatalysis: Mechanisms and Materials, *Chem. Rev.* **2014**, 114, 9919–9986
- [50] Xu, B.; Sohn, H.Y.; Mohassab, Y.; Lan, Y. Structures, preparation and applications of titanium suboxides, *RSC Adv.* **2016**, 6, 79706
- [51] Matsumoto, Y.; Yoshikawa, T.; Sato, E. Dependence of the Band Bending of the Oxide Semiconductors on pH, *J. Electrochem. Soc.* **1989**, 136(5), 1389
- [52] Trasatti, S. The Absolute Electrode Potential: an Explanatory Note, *International Union of Pure and Applied Chemistry, Pure & Appl. Chem.*, 1986, 58 (7), 955–66

- [53] Matsumoto, Y. Energy Positions of Oxide Semiconductors and Photocatalysis with Iron Complex Oxides, *J. Solid State Chem.* **1996**, 126, 227–234
- [54] Van de Krol, R.; Goossens, A.; Schoonman, J. Mott-Schottky Analysis of Nanometer-Scale Thin-Films Anatase TiO<sub>2</sub>. *J. Electrochem. Soc.* **1997**, 144, 1723–1727
- [55] Wang, C.; Chen, Z.; Jin, H.; Cao, C.; Li, J.; Mi, Z. Enhancing Visible-Light Photoelectrochemical Water Splitting Through Transition- Metal Doped TiO<sub>2</sub> Nanorod Arrays. *J. Mater. Chem. A* **2014**, 2, 17820–17827
- [56] Cardon, F.; Gomes, W. P. On the determination of the flat-band potential of a semiconductor in contact with a metal or an electrolyte from the Mott-Schottky plot, *Journal of Physics D: Applied Physics* **1987**, 11, L63
- [57] Xu, P.; Milstein, T.J.; Mallouk, T.E. Flat-Band Potentials of Molecularly Thin Metal Oxide Nanosheets, *ACS Appl. Mater. Interfaces* **2016**, 8, 11539–11547
- [58] Kavan, L.; Tétreault, N.; Moehl, T.; Grätzel, M. Electrochemical Characterization of TiO<sub>2</sub> Blocking Layers for Dye-Sensitized Solar Cells, *J. Phys. Chem. C* **2014**, 118, 16408–16418



338x190mm (96 x 96 DPI)